

July 2022

## Stellar Atmosphere Models for Select VERITAS Stellar Intensity Interferometry Targets

Jackson Ladd Sackrider  
sackrij1@my.erau.edu

Jason P. Aufdenberg  
Embry-Riddle Aeronautical University, aufded93@erau.edu

Katelyn Sonnen  
sonnenk1@my.erau.edu

Follow this and additional works at: <https://commons.erau.edu/beyond>

 Part of the [Cosmology, Relativity, and Gravity Commons](#), [Numerical Analysis and Scientific Computing Commons](#), [Other Astrophysics and Astronomy Commons](#), and the [Stars, Interstellar Medium and the Galaxy Commons](#)

---

### Recommended Citation

Sackrider, Jackson Ladd; Aufdenberg, Jason P.; and Sonnen, Katelyn (2022) "Stellar Atmosphere Models for Select VERITAS Stellar Intensity Interferometry Targets," *Beyond: Undergraduate Research Journal*: Vol. 6 , Article 6.  
Available at: <https://commons.erau.edu/beyond/vol6/iss1/6>

This Article is brought to you for free and open access by the Journals at Scholarly Commons. It has been accepted for inclusion in Beyond: Undergraduate Research Journal by an authorized administrator of Scholarly Commons. For more information, please contact [commons@erau.edu](mailto:commons@erau.edu).

---

## Stellar Atmosphere Models for Select VERITAS Stellar Intensity Interferometry Targets

### Cover Page Footnote

This work was supported by an ERAU Summer Undergraduate Research Fellowship to Jackson Sackrider. Thanks to Peter Hauschildt and Eddie Baron for advice on computing high-resolution synthetic spectra with PHOENIX with non-LTE helium lines. Based on spectral data retrieved from the ELODIE archive at Observatoire de Haute-Provence (OHP) and IACOB database. The IACOB spectroscopic database is based on observations made with the Nordic Optical Telescope operated by the Nordic Optical Telescope Scientific Association, and the Mercator Telescope, operated by the Flemish Community, both at the Observatorio de El Roque de Los Muchachos (La Palma, Spain) of the Instituto de Astrofísica de Canarias. This research has made use of the SIMBAD database, operated at CDS, Strasbourg, France. This work made use of Astropy (<http://www.astropy.org>) a community-developed core Python package and an ecosystem of tools and resources for astronomy (Astropy Collaboration et al. 2018, 2022).

# *Stellar Atmosphere Models for Select VERITAS Stellar Intensity Interferometry Targets*

Jackson Sackrider, Jason P. Aufdenberg Ph.D, Katelyn Sonnen  
*Embry-Riddle Aeronautical University, Department of Physical Sciences*  
*1 Aerospace Blvd, Daytona Beach, FL 32114, USA*

## **Abstract**

Since 2020 the Very Energetic Radiation Imaging Telescope Array System (VERITAS) has observed 48 stellar targets using the technique of Stellar Intensity Interferometry (SII). Angular diameter measurements by VERITAS SII (VSII) in a waveband near 400 nm complement existing angular diameter measurements in the near-infrared (near-IR). VSII observations will test fundamental predictions of stellar atmosphere models and should be more sensitive to limb darkening and gravity darkening effects than measurements in the near-IR; however, the magnitude of this difference has not been systematically explored in the literature. In order to investigate the synthetic interferometric (as well as spectroscopic) appearance of stars in the blue relative to the near-IR, grids of model atmospheres (3463 models in total) appropriate for six stars observed by VSII have been computed: four rapid rotators  $\alpha$  Cep,  $\alpha$  Leo,  $\alpha$  Lyr and  $\eta$  UMa, along with two slow rotators  $\beta$  UMa and  $\beta$  CMa. This paper presents synthetic spectra, model images, and visibility predictions for these stars and three others ( $\alpha$  Aql,  $\alpha$  Oph, and  $\beta$  Cas). It is predicted these stars will appear smaller in angular size and exhibit higher visibilities in the first lobe of the visibility curve at 400 nm relative to 1746 nm at the same spatial frequencies, consistent with expectations. VSII baselines see only the second and higher lobes of  $\alpha$  Lyr and  $\alpha$  Aql due to their large angular diameters.  $\alpha$  Aql is predicted to have a rich spectrum of visibilities in the third lobe, however the visibilities are very low. Synthetic spectra match archival spectra around 400nm best for  $\alpha$  Leo,  $\alpha$  Aql,  $\alpha$  Oph,  $\eta$  UMa and  $\beta$  CMa, while for  $\alpha$  Cep,  $\beta$  Cas, and  $\alpha$  Lyr synthetic spectra exhibit higher fluctuations in line strength than observed. A synthetic spectrum for  $\eta$  UMa provides a good match to the H $\delta$  line, but not for the adjacent He I lines. In addition to resolving the discrepancies between the synthetic and archival spectra, comparing our visibility predictions to VSII

## **Introduction**

The Very Energetic Radiation Imaging Telescope Array System (VERITAS), located at the Fred Lawrence Whipple Observatory in Arizona (31.6884° N, 110.8854° W), is the first experiment to routinely make observations using stellar intensity interferometry in the past 50 years. This array consists of four telescopes, creating six unique telescope pairs, resulting in six different interferometric baselines for the entire array. The VERITAS Stellar Intensity Interferometry (VSII) experiment (Abeysekara et al. 2020) is capable of taking observations in a band near

400 nm, thus VSII measurements are expected to be more sensitive to stellar surface intensity gradients than earlier near-infrared measurements. A change in stellar surface brightness associated with a temperature change is a strong function of wavelength, most easily demonstrated using the Rayleigh-Jeans approximation,

$$B_{\lambda}(T) = \frac{2ckT}{\lambda^4} \quad (1)$$

where  $B_{\lambda}(T)$  is the Planck function. Its partial derivative with respect to temperature,

$$\frac{\partial B}{\partial T} = \frac{2ck}{\lambda^4} \quad (2)$$

Table 1. Stellar Parameters For Rapid Rotators<sup>a</sup>

| Name         | Parallax <sup>b</sup><br>(mas) | $\theta_{\text{eq}}$ <sup>c</sup><br>(mas) | $i$ <sup>d</sup><br>( $^{\circ}$ ) | PA <sup>e</sup><br>( $^{\circ}$ ) | polar $T_{\text{eff}}$ <sup>f</sup><br>(K) | $\Delta T_{\text{eff}}$<br>(K) | Mass<br>$M_{\odot}$ | $\omega$ <sup>g</sup> | $\beta$ <sup>h</sup> | $v_{\text{eq}}$ <sup>i</sup><br>km s <sup>-1</sup> | Decl. (2000)<br>( $^{\circ}$ ) | R.A. (2000)                                     |
|--------------|--------------------------------|--|------------------------------------|-----------------------------------|--|--------------------------------|---------------------|-----------------------|----------------------|--|--------------------------------|---|
| $\alpha$ Cep | 66.50                          | 1.7  | 55.7                               | -178                              | 8588                                       | 1997                           | 1.72                | 0.94                  | 0.216                | 252  | +62.59                         | 21 <sup>h</sup> 18 <sup>m</sup> 35 <sup>s</sup> |
| $\alpha$ Aql | 194.95                         | 3.67                                       | 57.2                               | -62                               | 8450                                       | 1557                           | 1.95                | 0.92                  | 0.19                 | 295  | +08.87                         | 19 <sup>h</sup> 50 <sup>m</sup> 47 <sup>s</sup> |
| $\beta$ Cas  | 59.58                          | 2.10                                       | 18.2                               | -7                                | 7079                                       | 898                            | 2.27                | 0.89                  | 0.15                 | 217  | +59.15                         | 00 <sup>h</sup> 09 <sup>m</sup> 10 <sup>s</sup> |
| $\alpha$ Oph | 67.13                          | 1.80                                       | 87.7                               | -54                               | 9450                                       | 1242                           | 2.10                | 0.71                  | 0.16                 | 236  | +12.56                         | 17 <sup>h</sup> 34 <sup>m</sup> 56 <sup>s</sup> |
| $\alpha$ Leo | 41.13                          | 1.61                                       | 85.7                               | +258                              | 15070                                      | 3154                           | 4.26                | 0.84                  | 0.16                 | 243  | +11.97                         | 10 <sup>h</sup> 08 <sup>m</sup> 22 <sup>s</sup> |
| $\alpha$ Lyr | 130.23                         | 3.30                                       | 4.7                                | -58                               | 10070                                      | 1142                           | 2.40                | 0.77                  | 0.23                 | 205  | +38.78                         | 18 <sup>h</sup> 36 <sup>m</sup> 56 <sup>s</sup> |
| $\eta$ UMa   | 31.38                          | 0.834                                      | 23                                 | ...                               | 20000                                      | 5628                           | 6.1                 | 0.95                  | 0.25                 | 503  | +47.76                         | 13 <sup>h</sup> 47 <sup>m</sup> 32 <sup>s</sup> |

<sup>a</sup>Data sources: Alderamin ( $\alpha$  Cep) Zhao et al. (2009), Altair ( $\alpha$  Aql) Monnier et al. (2007), Caph ( $\beta$  Cas) Che et al. (2011), Rasalhague ( $\alpha$  Oph) Zhao et al. (2009), Regulus ( $\alpha$  Leo) Che et al. (2011), Vega ( $\alpha$  Lyr) (Monnier et al. 2012, concordance model), Alkaid ( $\eta$  UMa) (Stoekley & Buscombe 1987; Gordon et al. 2019, PA not constrained)

<sup>b</sup>van Leeuwen (2007)

<sup>c</sup>Equatorial angular diameter

<sup>d</sup>Inclination, zero degrees is the pole-on view.

<sup>e</sup>Position angle of rotational axis, zero degrees is the rotation axis aligned with north.

<sup>f</sup>Polar effective temperature

<sup>g</sup>Fraction of the critical angular break-up rate

<sup>h</sup>Gravity darkening parameter,  $\beta = 0.25$  according to von Zeipel (1924a,b), observations provide evidence for lower  $\beta$  values for faster rotation, supported by theory (Espinosa Lara & Rieutord 2011).

<sup>i</sup>Equatorial rotational velocity

is 363 times larger at 400 nm relative to the H-band at 1746 nm. Real stars are not black bodies and Rayleigh-Jeans approximation is not particularly good at 400 nm, but this quantitative example gives the magnitude of the brightness sensitivity to the temperature variations.

Three stars ( $\alpha$  Cep,  $\alpha$  Leo and  $\alpha$  Lyr) targeted by VSII are a subset of the six northern-hemisphere rapid rotators most extensively observed by long-baseline interferometry in the near-IR (see Table 1). The angular diameters of these stars' stellar equators range from 0.85 mas ( $\alpha$  Cep) to 3.30 mas ( $\alpha$  Lyr) and they have been extensively observed by Michigan Infrared Combiner (MIRC) with the Center for High Angular Resolution Astronomy (CHARA) Array in the near-infrared H-band (1.65  $\mu\text{m}$ ) split into eight spectral channels (Monnier et al. 2007; Zhao et al. 2009; Che et al. 2011; Monnier et al. 2012).

Rapid rotation produces a lower surface gravity at the equator relative to the pole, up to a factor of 4 or 0.6 dex lower among these stars, resulting in gravity darkening, a darkening in intensity due to the pole-to-equator temperature difference,  $\Delta T_{\text{eff}}$ . Among the six stars, models matching the CHARA/MIRC data have shown that Regulus has the largest  $\Delta T_{\text{eff}}$  (3154 K) and

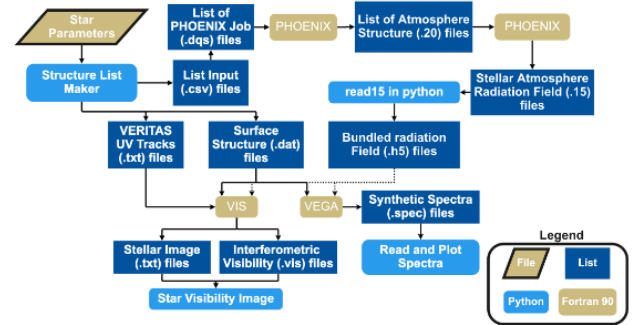


Figure 1: This flow chart is an attempt to capture the work flow between the workhorse Fortran codes PHOENIX and VIS, which compute the radiation fields and visibilities, and helper Python and Perl scripts which process and plot both input and output for the Fortran codes.

Caph the smallest ( $\Delta T_{\text{eff}} \approx 898$  K, see Table 1).

Before these observations, the pole-to-equator temperature variation was generally assumed to follow von Zeipel's law (von Zeipel 1924a,b),

$$T_{\text{eff}}(\vartheta) = T_{\text{eff pole}} \left( \frac{g_{\text{eff}}(\vartheta)}{g_{\text{pole}}} \right)^{\beta} \quad (3)$$

where  $\beta = 0.25$ . Model fits to CHARA/MIRC observations have yielded  $\beta$  values as low as  $0.15 \pm 0.01$  (see Che et al. (2011) and Table 1). Modern theory (Espinosa Lara & Rieutord 2011) predicts that as stars rotate faster, the value of  $\beta$  drops below 0.25.

For detailed predictions of the differences in interferometric observables expected between 400 nm and the H-band, model atmosphere structures have been converged, using the 1-D spherical mode of the PHOENIX stellar atmosphere code (Hauschildt & Baron 1999, 2010, 2014), using parameters which span the ranges of temperature, surface gravity and mass for the stars, see Table 2. Solar abundances are assumed, but can be later modified for a detailed analysis of each star. From these model structures, radiation field intensities, as a function of wavelength, temperature, surface gravity, and viewing angle, were extracted and interpolated onto a rotationally-distorted stellar surface. The work flow is outlined in Figure 1, for additional details see Aufdenberg et al. (2006).

The computation of the pole-to-equator run of temperature, gravity and velocity, the input list of grid parameters, the packing of the resultant radiation field data in the HDF5 (.h5) format, and the computation of  $u$ ,  $v$  tracks, following (Davis et al. 2020), were all done in Python, initially developed in Jupyter notebooks at CoCalc.com. Parallel Fortran 90 codes were used for the interpolation of the radiation field data (read from an .h5 file) onto the model stellar surfaces. The code VIS was used for the construction of the model image and the visibility computations while the code VEGA was used to compute high-dispersion spectra and spectral energy distributions.

## Fundamental Parameters and Equations for Rapidly-Rotating Stars

The run of radius, effective temperature and surface gravity, as a function of stellar co-latitude, necessary to create the monochromatic visibility predictions for the stars in Table 1 were calculated by the python program structure list maker.py. The program requires input parameters read from a local Stellar Database. These input variables are as follows:

1.  $T_{\text{eff}}^{\text{pole}}$ : the effective polar temperature,
2.  $\log(g)_{\text{pole}}$ : the effective polar gravity,
3.  $\theta_{\text{equ}}$ : the angular size of the equator in milliarcseconds,

4.  $\pi_{\text{hip}}$ : the trigonometric parallax in milliarcseconds,
5.  $\omega$ : the fraction of the critical angular break-up rate,
6.  $v \sin i$ : the observed projected rotational velocity in  $\text{km s}^{-1}$ ,
7.  $\beta$ : the gravity-darkening exponent.

Using these input parameters (see Table 1 for values), the model for each rapidly rotating star can be created.

The structure maker function begins, following Aufdenberg et al. (2006), with

$$R_{\text{eq}} = 107.48 \frac{\theta_{\text{eq}}}{\pi_{\text{hip}}} \quad (4)$$

where  $R_{\text{eq}}$  is the equatorial radius in solar units. Next, the polar radius is calculated in terms of the equatorial radius according to Cranmer & Owocki (1996),

$$R_{\text{pole}} = \frac{\omega R_{\text{equ}}}{3 \cos \left[ \frac{\pi + \cos^{-1}(\omega)}{3} \right]} \quad (5)$$

where  $R_{\text{pole}}$  is in solar units. Using  $R_{\text{pole}}$ , the stellar mass is then calculated using,

$$M = \frac{g_{\text{pole}} R_{\text{pole}}^2}{G} \quad (6)$$

where  $G$  is the universal gravitational constant ( $6.67430 \times 10^{-11} \text{ N m}^2 \text{ kg}^{-2}$ ),  $g_{\text{pole}}$  is the effective polar gravity and  $M$  is in solar masses. Luminosity, in solar luminosities, was then calculated using,

$$L = \frac{\sigma (T_{\text{eff}}^{\text{pole}})^4 \Sigma}{g_{\text{pole}}} \quad (7)$$

where  $\sigma$  is the Stefan-Boltzman constant and  $\Sigma$  is the surface-weighted gravity (Cranmer & Owocki 1996), calculated from:

$$\Sigma \approx 4\pi GM(1.0 - 0.19696\omega^2 - 0.094292\omega^4 + 0.33812\omega^6 - 1.30660\omega^8 + 1.8286\omega^{10} - 0.92714\omega^{12}) \quad (8)$$

The effective temperature as a function of surface gravity from von Zeipel's radiative law at all colatitudes  $\vartheta$  was calculated from:

$$T_{\text{eff}} = \left[ \frac{L}{\sigma \Sigma} g(\vartheta) \right]^{\beta} = T_{\text{eff}}^{\text{pole}} \left[ \frac{g(\vartheta)}{g_{\text{pole}}} \right]^{\beta}, \quad (9)$$

Table 2. Adopted model parameters for the CHARA/MIRC rapid rotators

| Name   | Unit               | $\alpha$ Cep | $\alpha$ Aql | $\beta$ Cas | $\alpha$ Oph | $\alpha$ Leo | $\alpha$ Lyr | $\eta$ UMa |
|--|--------------------|--------------|--------------|-------------|--------------|--------------|--------------|------------|
| Equatorial Diameter, $\theta_{\text{eq}}$                              | mas                | 1.700        | 3.67         | 2.100       | 1.800        | 1.610        | 3.300        | 0.834      |
| Fraction, critical angular breakup rate, $\omega/\omega_{\text{crit}}$ | ...                | 0.940        | 0.920        | 0.89        | 0.709        | 0.836        | 0.770        | 0.950      |
| Gravity-darkening exponent, $\beta$                                    | ...                | 0.216        | 0.19         | 0.15        | 0.16         | 0.16         | 0.23         | 0.250      |
| Polar effective temperature, $T_{\text{pol}}$                          | K                  | 8588.000     | 8450.000     | 7079.000    | 9450.000     | 15070.000    | 10070.000    | 20000      |
| Equatorial effective temperature, $T_{\text{eq}}$                      | K                  | 6591.468     | 6892.532     | 6181.389    | 8208.147     | 11916.377    | 8927.302     | 14372      |
| Pole to equator temperature difference, $\Delta T$                     | K                  | 1996.532     | 1557.358     | 897.611     | 1241.853     | 3153.623     | 1142.698     | 5628       |
| Polar surface gravity, $\log_{10}(g)_{\text{pol}}$                     | cgs                | 4.000        | 4.300        | 3.800       | 4.000        | 4.050        | 4.050        | 4.390      |
| Equatorial surface gravity, $\log_{10}(g)_{\text{eq}}$                 | cgs                | 3.468        | 3.834        | 3.407       | 3.618        | 3.413        | 3.823        | 3.816      |
| Polar radius, $R_{\text{pol}}$   | $R_{\odot}$        | 2.172        | 1.635        | 3.142       | 2.400        | 3.226        | 2.421        | 2.230      |
| Equatorial radius, $R_{\text{eq}}$                                     | $R_{\odot}$        | 2.748        | 2.023        | 3.788       | 2.822        | 4.207        | 2.724        | 2.857      |
| Radii ratio, $R_{\text{eq}}/R_{\text{pole}}$                           | ...                | 1.265        | 1.238        | 1.206       | 1.201        | 1.304        | 1.125        | 1.281      |
| Mass, $M$  | $M_{\odot}$        | 1.722        | 1.946        | 2.274       | 2.101        | 4.263        | 2.400        | 4.454      |
| Luminosity   | $L_{\odot}$        | 16.965       | 9.261        | 17.438      | 32.459       | 341.639      | 46.354       | 517.358    |
| Equatorial velocity, $V_{\text{eq}}$                                   | $\text{km s}^{-1}$ | 251.660      | 295.339      | 216.968     | 236.44       | 342.754      | 205.032      | 408.898    |
| Equatorial critical velocity, $V_{\text{eq-crit}}$                     | $\text{km s}^{-1}$ | 317.468      | 389.017      | 303.299     | 333.679      | 409.843      | 355.022      | 503.941    |
| Velocity ratio, $V_{\text{eq}} / V_{\text{eq-crit}}$                   | ...                | 0.793        | 0.759        | 0.715       | 0.709        | 0.836        | 0.578        | 0.811      |

where  $\beta$  is the gravity darkening coefficient. The effective temperature difference can be expressed simply as the difference of the effective polar temperature from the effective equatorial temperature, or more reliably in terms of the effective polar temperature and  $\omega$ ,

$$\Delta T_{\text{eff}} = T_{\text{eff}}^{\text{pole}} - T_{\text{eff}}^{\text{eq}} = T_{\text{eff}}^{\text{pole}} \left[ 1 - \left( \frac{\omega^2}{\eta^2} - \frac{8}{27} \eta \omega \right)^{\beta} \right] \quad (10)$$

where  $\eta$  can be calculated by

$$\eta = 3 \cos \left[ \frac{\pi + \cos^{-1}(\omega)}{3} \right] \quad (11)$$

The rotation rate can be related to the critical rotation rate by

$$\Omega = \omega \Omega_{\text{crit}} = \omega \left( \frac{8}{27} \frac{GM}{R_{\text{pole}}^3} \right)^{\frac{1}{2}} \quad (12)$$

Using the rotation rate, equatorial velocity and equatorial critical velocity can be calculated by

$$V_{\text{eq}} = R_{\text{eq}} \Omega \quad (13)$$

The effective gravity can be given as a function of  $\vartheta$  by

$$g(\vartheta) = \left[ g_r(\vartheta)^2 + g_{\vartheta}(\vartheta)^2 \right]^{\frac{1}{2}} \quad (14)$$

$$g_r(\vartheta) = -\frac{GM}{R(\vartheta)^2} + R(\vartheta)(\Omega \sin \vartheta)^2 \quad (15)$$

$$g_{\vartheta}(\vartheta) = R(\vartheta)\Omega^2 \sin \vartheta \cos \vartheta \quad (16)$$

where  $g_r$  and  $g_{\vartheta}$  are radial and colatitudinal components of the overall gravity field.

### 2.1. Computation of Synthetic Spectra

The synthetic spectrum flux at each wavelength  $\lambda$ ,  $F_{\lambda}$ , is computed from the interpolated intensity  $I_{\lambda}$  at each longitude  $\phi$  and co-latitude  $\vartheta$  on the stellar surface.

$$F(\lambda) = \int_0^{\pi} \int_0^{2\pi} -\frac{g(\vartheta)}{g_r(\vartheta)} I_{\lambda}(\vartheta, \phi) R(\vartheta)^2 \sin \vartheta \mu(\vartheta, \phi, i) d\phi d\vartheta \quad (17)$$

where  $\mu(\vartheta, \phi, i)$  is the angle between the stellar surface normal and the observer which is a function of the inclination,  $i$  as viewed from Earth.

### 2.2. Computation of Synthetic Visibilities

In order to calculate synthetic visibility values for comparison to forthcoming VSII observations, a two dimensional set of Fourier transforms was computed from

$$V_{\lambda}(u, v) = \int_{-\infty}^{\infty} \int_{-\infty}^{\infty} I_{\lambda}(x, y) e^{i2\pi(ux+vy)} dx dy \quad (18)$$

where the Fourier transform is calculated for each wavelength at each of the spatial frequency  $(u, v)$  coordinates (Aufdenberg et al. 2006). Each  $(u, v)$  coordinate corresponds to a projected baseline for a given latitude and hour angle:

$$u = B_E \cos h - B_N \sin b \sin h + B_U \cos b \sin h \quad (19)$$

$$v = B_E \sin \delta \sin h + B_N (\sin b \sin \delta \sin h + \cos b \cos \delta) - B_U (\cos b \sin \delta \sin h - \sin b \cos \delta) \quad (20)$$

where  $B_N$  and  $B_E$  are the North-South and East-West baseline components for each telescope pair,  $B_U$  is the elevation component for the pair,  $b$  are

the telescope's latitudes,  $h$  is the star's hour angle of the star, and  $\delta$  is the star's declination.

## Models for Individual Rapidly-Rotating Stars

### 2.1. Alderamin ( $\alpha$ Cephei)

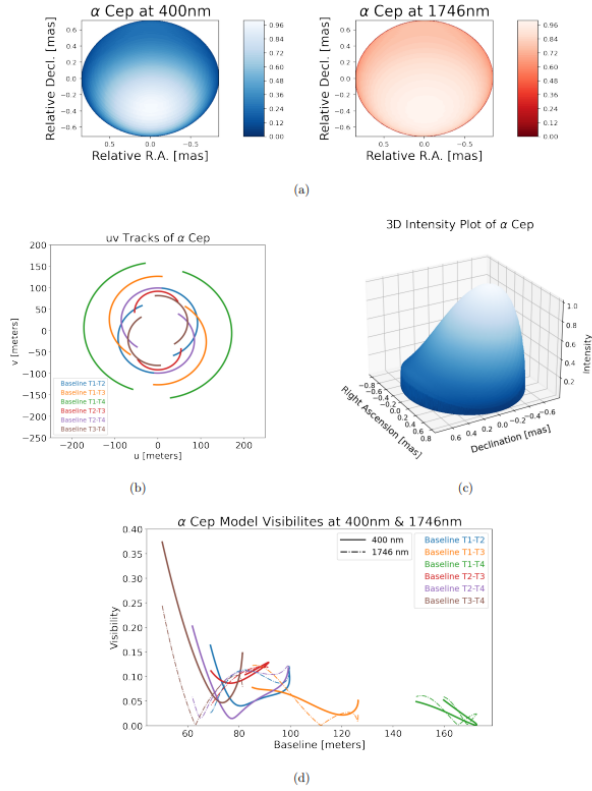


Figure 2: (a) Synthetic images at 400 nm and 1746nm, (b) VERITAS  $u, v$  tracks above  $20^\circ$  altitude, (c) Three dimensional intensity plot at 400 nm, and (d) visibilities at 400 nm and 1746 nm for  $\alpha$  Cephei).

Alderamin's fundamental parameters, computed using input values from Table 1 and Equations 4 to 16, are seen in Table 2. The numerical data table, showing values for the radius, effective temperature and surface gravity as a function of co-latitude is shown in Figure 2. This data table is used by both the VIS and VEGA Fortran programs, which synthetic images, visibilities and synthetic spectra are created, respectively.

Synthetic images for Alderamin in Figure 2a show a significant enhancement in surface-brightness contrast in the visible, 400 nm, relative to the near-infrared, 1746 nm. Alderamin has the highest declination ( $\delta = +62.59$ ) of the six

rapid-rotators and this affects the shape of the ( $u, v$ ) tracks in Figure 2b, which shows circular arcs for each projected baseline of each telescope pair. As Alderamin crosses the sky, its hour angle is shown from  $-5$  h to  $+5$  h. Alderamin has an equatorial velocity of  $251.66 \text{ km s}^{-1}$ , 94% of the critical angular breakup rate, and its pole is inclined  $55.7^\circ$  from Earth, resulting in the 3D brightness distribution plot in Figure 2c.

Figure 2d shows the interferometric visibility for Alderamin for each 10-hour ( $u, v$ ) track in Figure 2b. Telescope pair T3-T4 yields the lowest projected baseline on average for Alderamin since they have the shortest separation on the ground, 81.57 m. This pair has the lowest angular resolution, sampling the highest visibility values. In contrast, telescope pair T1-T4 has the largest separation, 172.61 m, and the highest angular resolution, sampling the highest spatial frequencies.

These model interferometric observables may be compared with VERITAS visibility estimates (forthcoming), testing the efficacy of the models produced by the pipeline.

Figure 11 shows a comparison between the synthetic spectrum of  $\alpha$  Cep and archival spectrum between 400 nm and 430 nm.

### 2.2. Altair ( $\alpha$ Aquilae)

Altair was one of the first interferometrically observed rotationally-distorted stars. Hanbury Brown et al. (1974) speculated that the star flattened based on measurements of its angular diameter. However, these researchers did not have adequate data to actually observe Altair's oblateness. Nearly 40 years later, Altair was observed to be rotationally flattened by the Palomar Testbed Interferometer (van Belle et al. 2001). Altair is one of the few stars to have its image taken; Monnier et al. (2007) obtained an image of it with MIRC on the CHARA Array interferometer, showing the effects of gravity darkening.

From the Monnier et al. (2007) beta-free model: The gravity darkening parameter  $\beta = 0.190 \pm 0.012$ , the equatorial velocity  $V_{\text{eq}} = 295 \text{ km s}^{-1}$ , which is 92% of the model's critical breakup rate, the inclination angle  $i = 57.2^\circ \pm 1.9^\circ$ , and

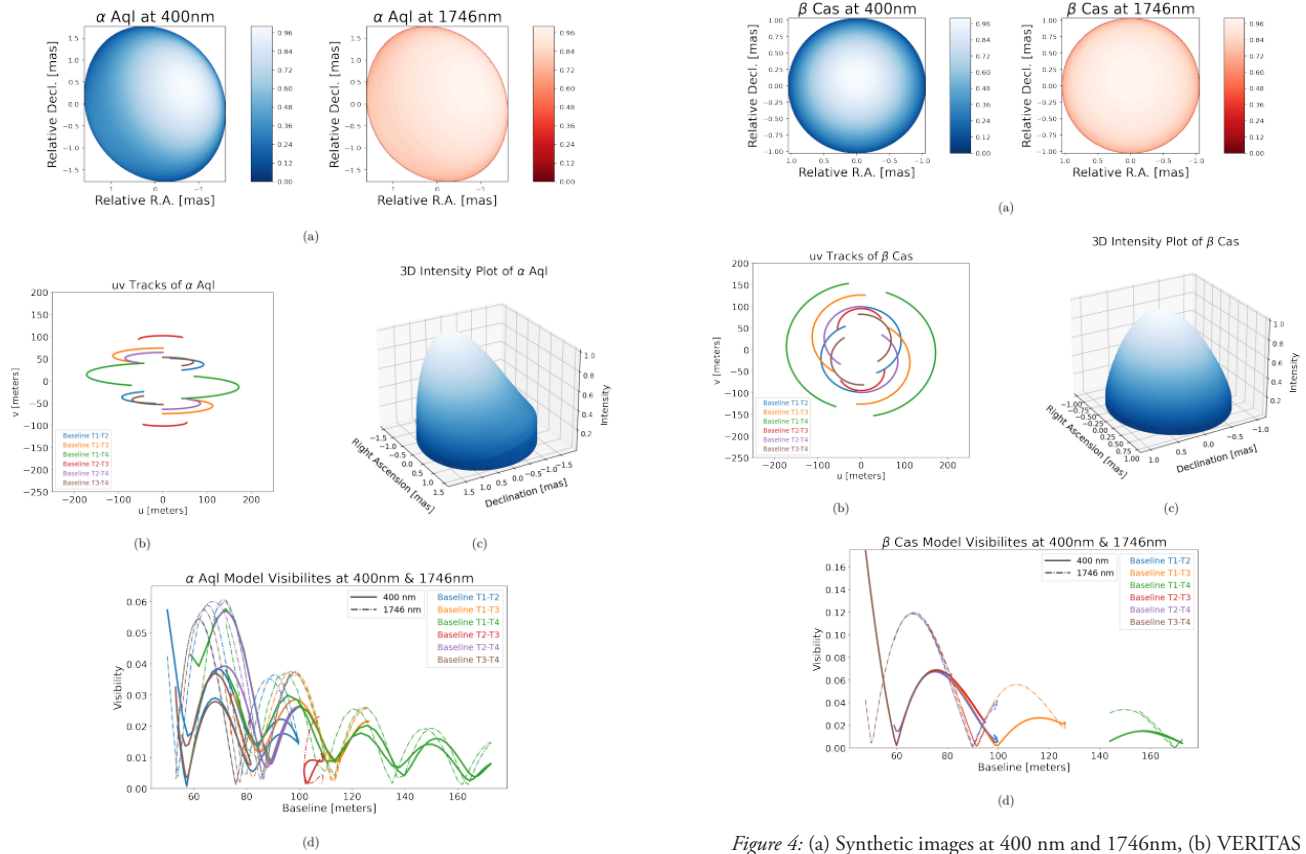


Figure 3: (a) Synthetic images at 400 nm and 1746nm, (b) VERITAS  $u$ ,  $v$  tracks above  $20^\circ$  altitude, (c) Three dimensional intensity plot at 400 nm, and (d) visibilities at 400 nm and 1746 nm for  $\alpha$  Aquilae.

the position angle  $PA = -61.8^\circ \pm 0.8^\circ$ . Figure 3a was constructed using the pipeline of programs seen in Figure 1. This model shows the surface-brightness contrast created by rapid rotation is consistent with the image from Monnier et al. (2007). In addition, Figure 3c shows the model 3D brightness distribution of the star on the sky. This model also shows the intense contrast between the visible pole and the equator. Figure 3d shows the model interferometric visibilities for all six baselines, the corresponding  $u$ ,  $v$  tracks are shown in Figure 3b. Figure 11 shows a comparison between the synthetic spectrum of  $\alpha$  Aql and archival spectrum between 400 nm and 430 nm.

### 2.3. Caph ( $\beta$ Cassiopeiae)

Caph is commonly known for being the second brightest Delta Scuti star in the sky, after Altair. This discovery was made by Millis (1966) at the Lowell Observatory in Arizona. Delta Scuti stars pulsate in radial and non-radial modes which

Figure 4: (a) Synthetic images at 400 nm and 1746nm, (b) VERITAS  $u$ ,  $v$  tracks above  $20^\circ$  altitude, (c) Three dimensional intensity plot at 400 nm, and (d) visibilities at 400 nm and 1746 nm for  $\beta$  Cassiopeiae).

Caph was once considered to be a spectroscopic binary, however a companion star was never found.

Caph has a relatively low inclination angle of  $18.2^\circ$ , which makes its center-to-limb intensity variation nearly circularly symmetric. Figure 4a shows the predicted surface-brightness contrast for the rapid rotator, with Caph's higher intensity pole near the center and its lower intensity equator near the limb. This contrast is visualized in 3D in Figure 4c. Caph's declination is  $\delta = +59.15^\circ$ , resulting in much more rounded  $uv$ -tracks as seen in Figure 4b, as compared to a star with a lower declination, such as Altair in Figure 3b. Figure 4d shows the model interferometric visibilities for Caph for all six VSII baselines.

### 2.4. Rasalhague ( $\alpha$ Ophiuchi)

Rasalhague is the primary star of the binary system  $\alpha$  Ophiuchi (Wagman 1946). The orbital period was constrained by McCarthy (1983) to be 8.62 years. Little is known about the companion besides its mass (Gatewood 2005). Rasalhague is an

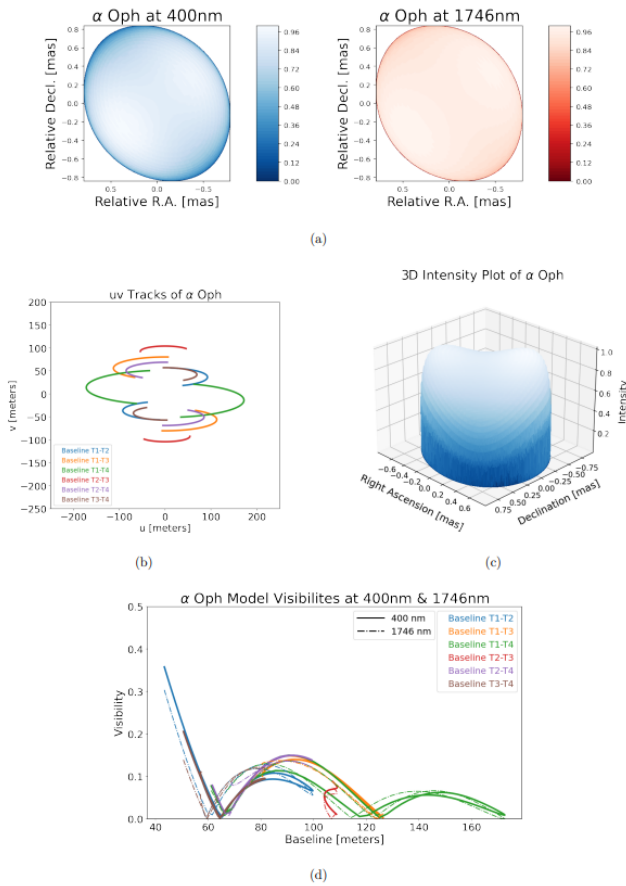


Figure 5: (a) Synthetic images at 400 nm and 1746nm, (b) VERITAS  $u$ ,  $v$  tracks above  $20^\circ$  altitude, (c) Three dimensional intensity plot at 400 nm, and (d) visibilities at 400 nm and 1746 nm for  $\alpha$  Ophiuchi).

caused by the effects of rapid rotation was fully shown once it was interferometrically imaged by Monnier et al. (2007).

Rasalhague has an inclination of  $87.7^\circ$ , making it a nearly equator-on rapid-rotator. With a position angle of  $-54^\circ$ , Figure 5a was created, which shows both bright poles and the gravity darkened equator. Figure 5c, the three-dimensional brightness distribution, shows in greater detail the bright poles compared to the less intense equator created by gravity-darkening. With a relatively low declination of  $12.56^\circ$ , Figure 5b shows the oval  $uv$ -tracks as its hour angle changes for VERITAS. Figure 5d shows the model interferometric visibilities, allowing for comparison of the models to observations.

### 2.5. Regulus ( $\alpha$ Leonis)

Regulus is a quadruple star system composed of

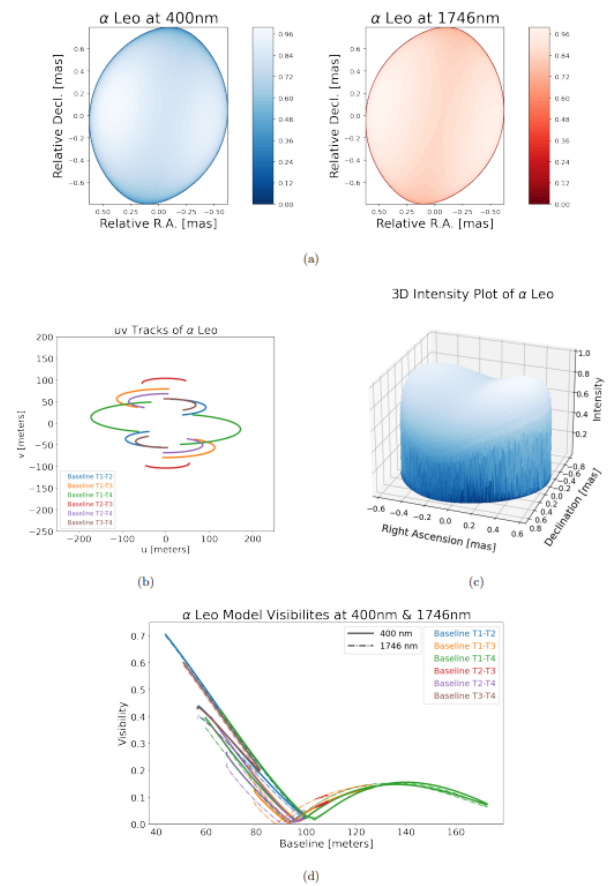


Figure 6: (a) Synthetic images at 400 nm and 1746nm, (b) VERITAS  $u$ ,  $v$  tracks above  $20^\circ$  altitude, (c) Three dimensional intensity plot at 400 nm, and (d) visibilities at 400 nm and 1746 nm for  $\alpha$  Leonis).

brightest of the four, is the rapidly-rotating main-sequence star with a companion, yet to be observed, but assumed to be a much fainter white dwarf. The two, Aa and Ab, take about 40.11 days to orbit around their center of mass, as constrained by Rappaport et al. (2009). Regulus A was originally theorized to be relatively young, however, its companion being a white dwarf suggests the binary system to be much older. Regulus C, a M4V star, is the faintest of the observed and has Regulus B, a K2V star as its companion. Tokovinin (1997) predicted that the two have an orbital period of about 600 years around their center of mass. Regulus A, the dominant and brightest, star in the  $\alpha$  Leonis system, exhibits intense gravity-darkening caused by its exceedingly rapid rotation, making it a star of interest for modeling.

Similarly to Rasalhague, Regulus A is a nearly equator-on rapid rotator, with an inclination

of  $85.7^\circ$ . Brightness distribution plots, shown in Figure 6a, reveal the intense oblateness ( $R_{\text{eq}} / R_{\text{pole}} = 1.3$ , see Table 2), two bright poles and dark equator as expected due to gravity darkening. Figure 6c shows the three-dimensional brightness distribution plot, exemplifying the higher intensity poles compared to the lower intensity equator. With a relatively low declination of  $+11.97^\circ$ , Regulus has much narrower  $uv$  tracks as seen from VIIS in Figure 6b. Figure 6d shows the model interferometric visibilities as Regulus transits above VERITAS, allowing for comparison of the models to observations.

### 2.6. Vega ( $\alpha$ Lyrae)

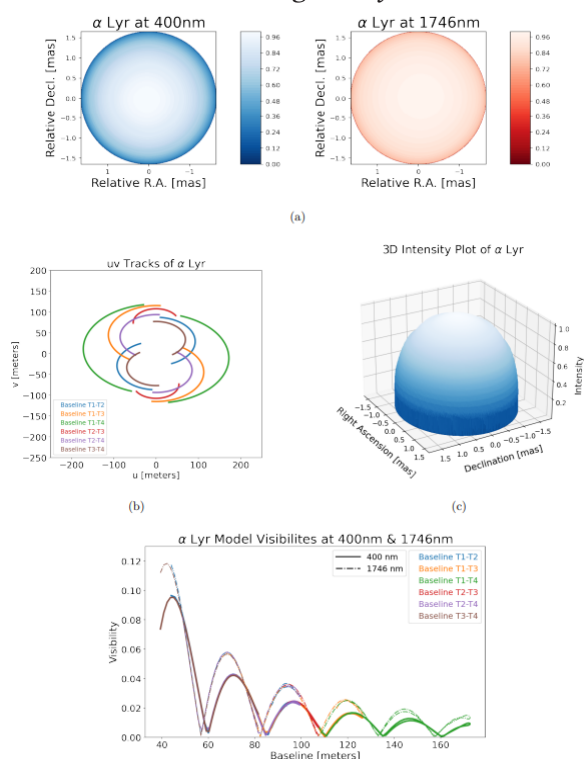


Figure 7: (a) Synthetic images at 400 nm and 1746nm, (b) VERITAS  $u$ ,  $v$  tracks above  $20^\circ$  altitude, (c) Three dimensional intensity plot at 400 nm, and (d) visibilities at 400 nm and 1746 nm for  $\alpha$  Lyrae).

Vega's narrow spectral lines led many researchers to believe it exhibited slow rotation, however, Vega's abnormal brightness as compared to other A0V stars led to speculation that it is rapidly rotating. When it was found that its weak line profiles had flat bottoms, consistent with rapid rotation (Hill et al. 2004), the phenomena arose that it was a pole-on rapid rotator. Vega also exhibits much stronger limb darkening for its spectral type, leading researchers to model the star

as a gravity-darkened rapid rotator (Aufdenberg et al. 2006; Peterson et al. 2006). In recent observations by the CHARA array, it was seen that Vega exhibited gravity-darkened limbs.

Vega has an inclination of  $4.7^\circ$ , making it a nearly pole-on rapid rotator. For this reason, Vega's center-to-limb intensity variation appears nearly symmetric. Figure 7a shows the expected surface-brightness contrast, as the visibility distribution at 400 nm heavily contrasts the bright pole to the gravity-darkened limbs at the equator. Figure 7b shows the  $uv$ -tracks of Vega as it transits over Mount Hopkins, AZ. Figure 7c shows the 3D brightness distribution of Vega, appearing relatively uniform due to its low inclination. A nearly pole-on view on Vega makes it appear circular, with the same angular size at every position angle, resulting in smooth, not double-valued visibilities as seen in Figure 7d.

### 2.7. Alkaid ( $\eta$ Ursae Majoris)

Alkaid is the hottest rapid rotator modeled so far with a polar effective temperature of 20000 K (see Table 2). It is also the smallest in angular size ( $\theta_{\text{eq}} = 0.834$  mas, see Table 2) and has not been imaged by CHARA/MIRC. Figure 8a shows the expected surface brightness contrast at 400 nm compared to 1746 nm. Figure 8b shows the  $uv$ -tracks of Alkaid as it transits over the VERITAS array. Figure 8c shows the three-dimensional brightness distribution plot, showing the effects of limb darkening and gravity darkening on the star. Figure 8d shows the predicted model visibilities. The position angle of the pole is not tightly constrained (Stoekley & Buscombe 1987), the model shown has  $\text{PA}=3^\circ$ .

## Models for Individual Slowly-Rotating Stars

The same pipeline used for rapidly-rotating stars can be utilized to model slowly-rotating stars. Modeling slowly-rotating stars is simplified by the star's lack of significant rotational distortion, for example  $\beta$  UMa is expected to exhibit only 0.5% variation in the angular size viewed equator-on, so the Von Zeipel effect is insignificant. The very

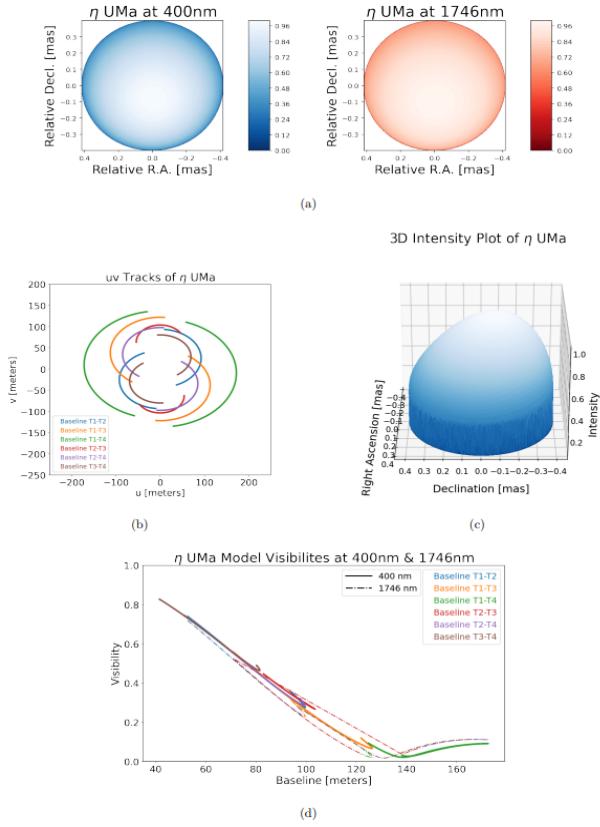


Figure 8: (a) Synthetic images at 400 nm and 1746nm, (b) VERITAS  $u, v$  tracks above  $20^\circ$  altitude, (c) Three dimensional intensity plot at 400 nm, and (d) visibilities at 400 nm and 1746 nm for  $\eta$  Ursae Majoris).

the position angle for the pole is not required. The fraction of critical angular rotation  $\omega$  is fixed to a value such that its equatorial velocity is equal to the measured  $v \sin i$  when  $i = 90^\circ$ . The temperature difference ( $\Delta T$ ) between pole and equator is very small, for example for  $\beta$  UMa it is 6 K. Slowly rotating B- and A-type stars fail to exhibit effects of gravity darkening, they should have nearly uniform gravity and temperature over their surface, though  $\beta$  UMa does exhibit non-radial pulsations, which introduce small fluctuations which are not modeled. Although these stars lack gravity darkening, they still exhibit the effects of limb darkening, which is wavelength dependent.

### 3.1. Merak ( $\beta$ Ursae Majoris)

Merak is a relatively slow-rotating subgiant star observed by VERITAS. Observations of the star in the infrared shows excess emissions, hinting towards the existence of a debris disk around it, much like the star Vega (Wyatt et al. 2007).

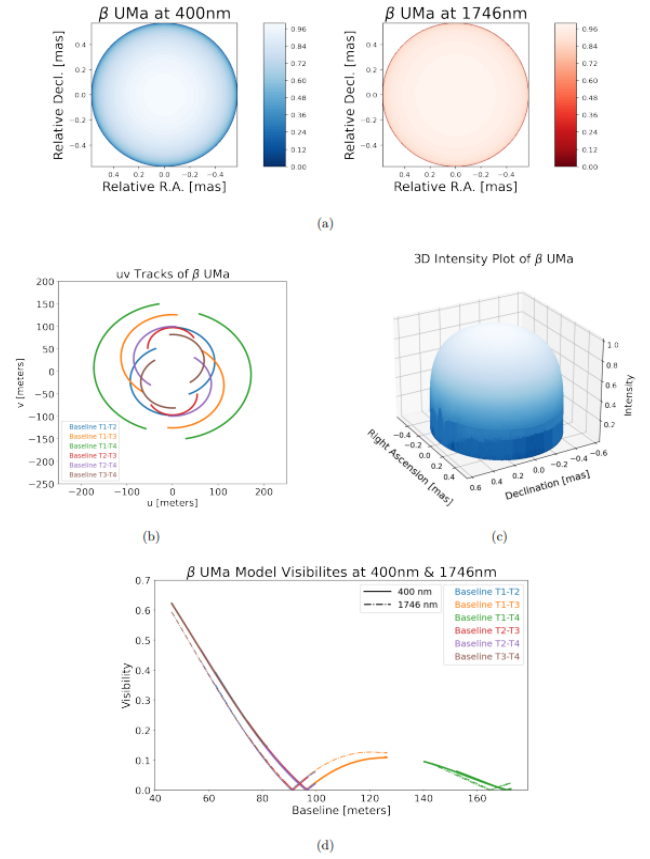


Figure 9: (a) Synthetic images at 400 nm and 1746nm, (b) VERITAS  $u, v$  tracks above  $20^\circ$  altitude, (c) Three dimensional intensity plot at 400 nm, and (d) visibilities at 400 nm and 1746 nm for  $\beta$  Ursae Majoris).

Merak's apparent slow rotation ( $V_{\text{eq}} \sin i = 45 \text{ km s}^{-1}$ ) (Adelman 1996) prevents the star from exhibiting effects of gravity darkening and it is predicted to display a limb-darkened disk as seen in Figure 9a. This is different from rapidly-rotating stars such as Vega, which can be seen in Figure 7a, where the limb and gravity darkening are both present. The 3D-brightness distribution is symmetrical compared to rapidly rotating stars, as seen by Figure 9c. Merak's  $uv$ -tracks for VIIS are shown in Figure 9b. Due to the slow rotation, its visibilities are only affected by limb darkening, stronger at 400 nm relative to 1746 nm, as shown in Figure 9d.

### 3.2. Mirzam ( $\beta$ Canis Majoris)

As shown in Table 4, Mirzam, the apparently slowest rotating star modeled in the project, has a projected rotational velocity of  $V_{\text{eq}} \sin i = 24 \text{ km s}^{-1}$ . It also exhibits high temperatures where the model  $T_{\text{eff}} = 24000 \text{ K}$ . This slow rotation and high

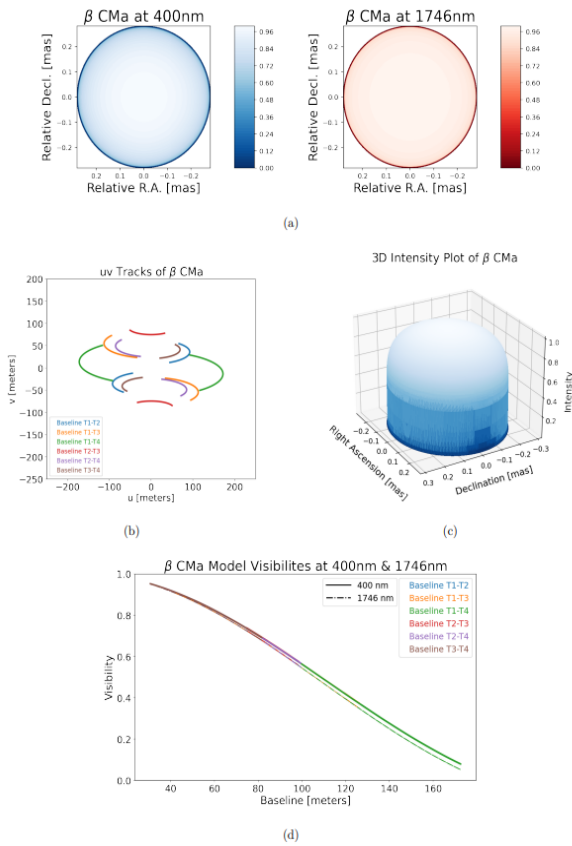


Figure 10: (a) Synthetic images at 400 nm and 1746nm, (b) VERITAS  $u, v$  tracks above  $20^\circ$  altitude, (c) Three dimensional intensity plot at 400 nm, and (d) visibilities at 400 nm and 1746 nm for  $\beta$  Canis Majoris.

temperature combination leads to a relatively low center-to-limb brightness ratio, as seen in Figure 10a. In addition, the 3D brightness distribution plot exemplifies this low ratio, creating a nearly flat-topped profile, shown by Figure 10c. Mirzam has a low declination of  $-17.95^\circ$ , making its T2-T3  $uv$ -tracks appear nearly convex as it transits above VERITAS, visualized in Figure 10b. This also leads the star to have a smoothed model visibility plot, with little to no difference between 400 nm and 1746 nm, as seen in Figure 10d.

### Comparison of Models to Archival Spectrum

In order to create an efficient and reliable pipeline of modeling programs, it is important to ensure the efficacy of the models. Not only does this ensure that the input parameters are consistent with reality, it also checks that the programs are working as intended. One way to do this is to

compare a model spectrum, created with the same parameters used to compute the model visibilities, to an archival spectrum. The model spectra are created by the VEGA Fortran 90 program, part of the pipeline shown in Figure 1. The model spectra are then normalized and compared to archival spectra using a Python script.

By comparing each model spectrum to an archival spectrum, the efficacy of the model parameters can be ascertained. When the model spectrum fits well, it is hoped that the model visibilities will more accurately predicted the forthcoming VSII observations.

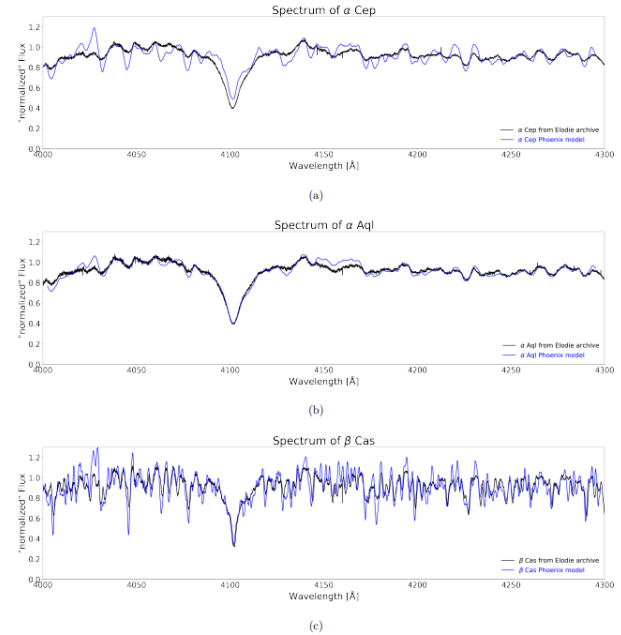


Figure 11: Synthetic spectra compared to archived spectra for stars  $\alpha$  Cep,  $\alpha$  Aql, and  $\beta$  Cas. The archived spectra was obtained through Elodie (see Table 6).

For example, the model spectrum for Alderamin is a loose fit to the archived Elodie spectrum as the model under exaggerates the Hydrogen  $\delta$  line. In contrast, the star Altair proves to be a much better fit, nearly matching the observed Hydrogen  $\delta$  line. Caph's strong spectral lines due to its pole-on inclination and low temperatures makes it challenging to model, this caused the PHOENIX program to over exaggerate some of Caph's already strong spectral lines. From these three stars, whose spectral plots are shown in Figure 11, it can be expected that Altair's model will have the best fit to VIIS visibilities.

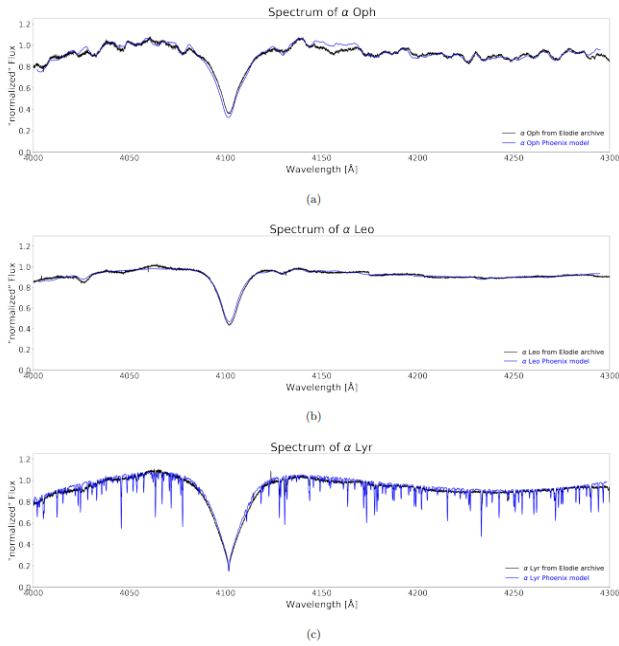


Figure 12: Synthetic spectra compared to archived spectra for stars  $\alpha$  Oph,  $\alpha$  Leo, and  $\alpha$  Lyr. The archived spectra was obtained through Elodie (see Table 6).

The model spectrum for Rasalhague fits relatively well, although the model overexaggerates the hydrogen line. The model spectrum for Regulus fits smoothly to the archived spectrum. Regulus is an exceedingly hot star, which allows for the ionization of many chemicals, creating a much smoother spectrum compared to other stars. Vega has much narrower spectral lines due to its nearly pole-on view, creating a much stronger absorption line for Hydrogen  $\delta$ . The model spectrum for Vega fits the archived Elodie spectrum closely, however it exaggerates many of the absorption lines. These three stars, Rasalhague, Regulus, and Vega have a model spectrum that closely fits Elodie archive spectra. It is expected that these star's model visibilities will closely resemble VIIS observations. The three spectra comparisons can be found in Figure 12.

The model spectrum for the chemically peculiar Merak fits exceedingly well, making it the best fit out of all the stars modeled. For this reason, it is expected to be one of the best fits to VIIS observations. In addition, Mirzar's model spectrum fits the archived spectrum closely as well, nearly perfectly after its Hydrogen  $\delta$  line. Similar to Regulus,  $\eta$  UMa has a smooth spectrum due to the ionization from the exceedingly high temperatures

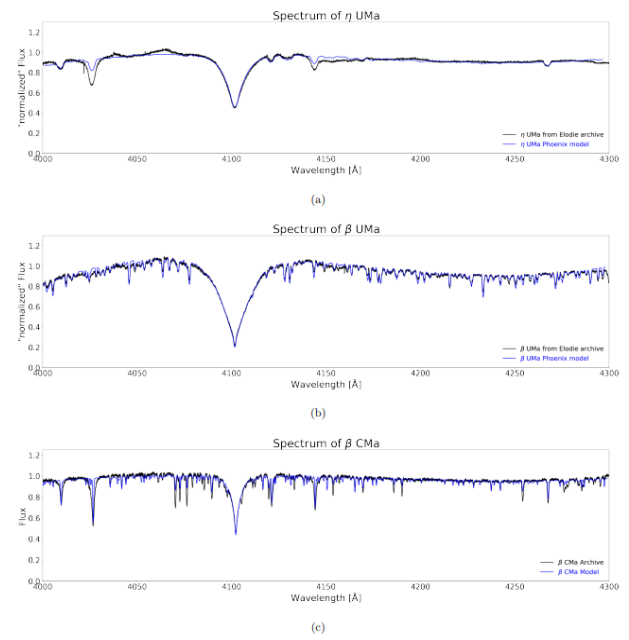


Figure 13: Synthetic spectra compared to archived spectra for stars  $\eta$  UMa,  $\beta$  UMa, and  $\beta$  CMa. The archived spectra was obtained through Elodie (see Table 6).

The model spectrum of  $\eta$  UMa falls short from the ionization of helium. The three spectra comparisons can be found in Figure 13.

## Conclusions and Future Work

It is predicted these stars will appear smaller and exhibit higher visibilities in the first lobe of the visibility curve at 400 nm relative to 1746 nm at the same spatial frequencies, consistent with our expectations. This contrast is best seen by  $\alpha$  Cep in Figure 2d where the 400 nm visibilities are nearly twice those at 1746 nm in the first lobe on the shortest (T3-T4) baseline. VSII baselines see only the second and higher lobes of  $\alpha$  Lyr and  $\alpha$  Aql due to their large angular diameters, where ( $\theta_{\text{Lyr}} = 3.30$  mas and  $\theta_{\text{Aql}} = 3.67$  mas).  $\alpha$  Aql is predicted to have a rich spectrum of visibilities in the third lobe for VSII's six telescope pairs, however the visibilities are very low ( $V < 0.06$ ,  $V^2 < 0.0036$ ). Synthetic spectra match archival spectra in the 400 nm to 430 nm band best for  $\alpha$  Leo,  $\alpha$  Aql,  $\alpha$  Oph,  $\beta$  UMa and  $\beta$  CMa, while synthetic spectra for  $\alpha$  Cep,  $\beta$  Cas, and  $\alpha$  Lyr exhibit higher fluctuations in line strength than observed. The synthetic spectrum for the rapid rotator  $\eta$  UMa provides a good match to the H  $\delta$  line, but for the adjacent

He I lines at 402.6 nm and 414.3 nm the synthetic lines are too weak. In addition to resolving the discrepancies between the synthetic and archival spectra, comparing our visibility predictions to VSII observations is anticipated in the near future. In addition, it is foreseen that the pipeline as shown in Figure 1 will be enhanced to feature more autonomous components, requiring less user interaction and debugging. Work continues on the VIS program to include wavelength-parallelization and better integration with the pipeline. Continuing on, model visibilities are expected to be produced for Zeta Oph and Gamma Cas as VSII anticipates observations in the coming seasons. This will ensure that as the pipeline progresses it remains functional and accurate, with new models built to match VSII targets.

## References

- Abeyssekara, A. U., Benbow, W., Brill, A., et al. 2020, *Nature Astronomy*, 4, 1164 doi:10.1038/s41550-020-1143-y
- Adelman, S. J. 1996, *MNRAS*, 280, 130. doi:10.1093/mnras/280.1.130
- Astropy Collaboration, Price-Whelan, A. M., Sipocz, B. M., et al. 2018, *AJ*, 156, 123. doi:10.3847/1538-3881/aabc4f
- Astropy Collaboration, Price-Whelan, A. M., Lim, P. L., et al. 2022, *ApJ*, 935, 167 doi:10.3847/1538-4357/ac7c74
- Aufdenberg, J. P., Hauschildt, P. H., & Baron, E. 1999, *MNRAS*, 302, 599. doi:10.1046/j.1365-8711.1999.02140.x
- Aufdenberg, J. P., Merand, A., Coude du Foresto, V., et al. 2006, *ApJ*, 645, 664. doi:10.1086/504149
- Boyajian, T. S., McAlister, H. A., van Belle, G., et al. 2012, *ApJ*, 746, 101. doi:10.1088/0004-637X/746/1/101
- Bursens, S., Simon-Diaz, S., Bowman, D. M., et al. 2020, *A&A*, 639, A81. doi:10.1051/0004-6361/202037700
- Che, X., Monnier, J. D., Zhao, M., et al. 2011, *ApJ*, 732, 68. doi:10.1088/0004-637X/732/2/68
- Cranmer, S. R. & Owocki, S. P. 1996, *ApJ*, 462, 469. doi:10.1086/177166
- Davis, J. D., Matthews, N. K., & Kieda, D. B. 2020, *Journal of Astronomical Telescopes, Instruments, and Systems*, 6, 037001. doi:10.1117/1.JATIS.6.3.037001
- Espinosa Lara, F. & Rieutord, M. 2011, *A&A*, 533, A43. doi:10.1051/0004-6361/201117252
- Gatewood, G. 2005, *AJ*, 130, 809. doi:10.1086/431723
- Gordon, K. D., Gies, D. R., Schaefer, G. H., et al. 2019, *ApJ*, 873, 91. doi:10.3847/1538-4357/ab04b2
- Hanbury Brown, R., Davis, J., & Allen, L. R. 1974, *MNRAS*, 167, 121. doi:10.1093/mnras/167.1.121
- Hauschildt, P. H., & Baron, E. 1999, *Journal of Computational and Applied Mathematics*, 109, 41. doi:10.1016/S0377-0427(99)00153-3
- Hauschildt, P. H., & Baron, E. 2010, *A&A*, 509, A36. doi:10.1051/0004-6361/200913064
- Hauschildt, P. H., & Baron, E. 2014, *A&A*, 566, A89. doi:10.1051/0004-6361/201423574
- Hill, G., Gulliver, A. F., & Adelman, S. J. 2004, *The A-Star Puzzle*, 224, 35. doi:10.1017/S1743921304004351
- McCarthy, D. W. 1983, *IAU Colloq. 76: Nearby Stars and the Stellar Luminosity Function*, 107 Millis, R. L. 1966, *PASP*, 78, 340. doi:10.1086/128361
- Monnier, J. D., Che, X., Zhao, M., et al. 2012, *ApJL*, 761, L3. doi:10.1088/2041-8205/761/1/L3
- Monnier, J. D., Zhao, M., Pedretti, E., et al. 2007, *Science*, 317, 342. doi:10.1126/science.1143205

- Moultaka, J., Ilovaisky, S. A., Prugniel, P., et al.  
2004, *PASP*, 116, 693.  
doi:10.1086/422177
- Peterson, D. M., Hummel, C. A., Pauls, T.  
A., et al. 2006, *Nature*, 440, 896.  
doi:10.1038/nature04661
- Rappaport, S., Podsiadlowski, P., & Horev,  
I. 2009, *ApJ*, 698, 666. doi:10.1088/0004-  
637X/698/1/666
- Simon-Díaz, S., Castro, N., Garcia, M., et al.  
2011, *Bulletin de la Societe Royale des  
Sciences de Liege*, 80, 514
- Simon-Díaz, S., Garcia, M., Herrero, A., et  
al. 2011, *Stellar Clusters & Associations: A  
RIA Workshop on Gaia*, 255
- Simon-Díaz, S., Negueruela, I., Maiz Apellaniz,  
J., et al. 2015, *Highlights of Spanish  
Astrophysics VIII*, 576
- Stoeckley, T. R. & Buscombe, W. 1987,  
*MNRAS*, 227, 801. doi:10.1093/  
mnras/227.4.801
- Tokovinin, A. A. 1997, *A&AS*, 124, 75.  
doi:10.1051/aas:1997181
- van Belle, G. T., Ciardi, D. R., Thompson, R. R.,  
et al. 2001, *ApJ*, 559, 1155.  
doi:10.1086/322340
- van Leeuwen, F. 2007, *A&A*, 474, 653.
- von Zeipel, H. 1924, *MNRAS*, 84, 665.  
doi:10.1093/mnras/84.9.665
- von Zeipel, H. 1924, *MNRAS*, 84, 684.  
doi:10.1093/mnras/84.9.684
- Wagman, N. E. 1946, *AJ*, 52, 50.  
doi:10.1086/105945
- Wyatt, M. C., Smith, R., Su, K. Y. L., et al.  
2007, *ApJ*, 663, 365. doi:10.1086/518404
- Zhao, M., Monnier, J. D., Pedretti, E., et  
al. 2009, *ApJ*, 701, 209.  
doi:10.1088/0004-637X/701/1/209

## Appendix

Table 3. Model Atmosphere Grid Parameters<sup>a</sup>

| Name         | max $T_{\text{eff}}$<br>(K) | min $T_{\text{eff}}$<br>(K) | step size<br>(K) | max $\log(g)$<br>$\text{cm s}^{-2}$ | min $\log(g)$<br>$\text{cm s}^{-2}$ | step size<br>$\text{cm s}^{-2}$ | $\xi^b$<br>$\text{km s}^{-1}$ | Mass<br>$M_{\odot}$ | N(models) |
|--------------|-----------------------------|-----------------------------|------------------|-------------------------------------|-------------------------------------|---------------------------------|-------------------------------|---------------------|-----------|
| $\alpha$ Cep | 8590                        | 6590                        | 50               | 4.05                                | 3.50                                | 0.05                            | 2                             | 1.92                | 492       |
| $\alpha$ Aql | 8450                        | 6850                        | 50               | 4.30                                | 3.80                                | 0.05                            | 2                             | 1.95                | 363       |
| $\beta$ Cas  | 7170                        | 6150                        | 30               | 3.80                                | 3.30                                | 0.05                            | 2                             | 2.27                | 385       |
| $\alpha$ Oph | 9450                        | 7450                        | 50               | 4.00                                | 3.60                                | 0.05                            | 2                             | 2.10                | 369       |
| $\alpha$ Leo | 15070                       | 10920                       | 40               | 4.05                                | 3.40                                | 0.05                            | 2                             | 4.20                | 1176      |
| $\alpha$ Lyr | 10100                       | 8900                        | 50               | 4.05                                | 3.75                                | 0.05                            | 2                             | 2.15                | 175       |
| $\eta$ UMa   | 20070                       | 14370                       | 100              | 4.41                                | 3.81                                | 0.10                            | 2                             | 4.50                | 406       |
| $\beta$ CMa  | 24000                       | 23960                       | 8                | 3.51                                | 3.49                                | 0.01                            | 2                             | 4.45                | 15        |
| $\beta$ UMa  | 9600                        | 9540                        | 20               | 3.92                                | 3.91                                | 0.01                            | 2                             | 2.70                | 28        |

<sup>a</sup>Input for PHOENIX stellar atmosphere models Hauschildt Baron (1999, 2010, 2014)<sup>b</sup>micro-turbulent velocityTable 4. Stellar Parameters for Slow Rotators<sup>a</sup>

| Name        | Parallax <sup>b</sup><br>(mas) | $\theta_{\text{eq}}^c$<br>(mas) | $T_{\text{eff}}^d$<br>(K) | Mass<br>( $M_{\odot}$ ) | $\log_{10}(g)^e$<br>(cgs) | $v \sin i^f$<br>( $\text{km s}^{-1}$ ) | Declination<br>( $^{\circ}$ ) | RA (2000)                                       |
|-------------|--------------------------------|---------------------------------|---------------------------|-------------------------|---------------------------|--|-------------------------------|---|
| $\beta$ UMa | 40.90                          | 1.149                           | 9600                      | 2.7                     | 3.92                      | 45                                     | +56.73                        | 11 <sup>h</sup> 01 <sup>m</sup> 50 <sup>s</sup> |
| $\beta$ CMa | 6.62                           | 0.565                           | 24000                     | 13.5                    | 3.50                      | 24                                     | -17.95                        | 06 <sup>h</sup> 22 <sup>m</sup> 42 <sup>s</sup> |

<sup>a</sup>Data sources:  $\beta$  UMa Adelman (1996);  $\beta$  CMa Aufdenberg et al. (1999)<sup>b</sup>From the High Precision Parallax Collecting Satellite van Leeuwen (2007)<sup>c</sup>Angular diameter:  $\beta$  UMa Boyajian et al. (2012);  $\beta$  CMa Aufdenberg et al. (1999)<sup>d</sup>Effective temperature<sup>e</sup>Surface gravity<sup>f</sup>Projected rotation velocity:  $\beta$  CMa Burssens et al. (2020)

## Appendix

Table 5. Adopted model parameters for slow rotators

| Name   | Unit               | $\beta$ UMa | $\beta$ CMa |
|--|--------------------|-------------|-------------|
| Equatorial Diameter, $\theta_{\text{eq}}$                              | mas                | 1.149       | 0.565       |
| Fraction, critical angular breakup rate, $\omega/\omega_{\text{crit}}$ | ...                | 0.200       | 0.100       |
| Gravity-darkening exponent, $\beta$                                    | ...                | 0.250       | 0.250       |
| Polar effective temperature, $T_{\text{pol}}$                          | K                  | 9600.000    | 24000.000   |
| Equatorial effective temperature, $T_{\text{eq}}$                      | K                  | 9542.161    | 23964.299   |
| Pole to equator temperature difference, $\Delta T$                     | K                  | 57.839      | 35.701      |
| Polar surface gravity, $\log_{10}(g)_{\text{pol}}$                     | cgs                | 3.920       | 3.500       |
| Equatorial surface gravity, $\log_{10}(g)_{\text{eq}}$                 | cgs                | 3.910       | 3.497       |
| Polar radius, $R_{\text{pol}}$   | $R_{\odot}$        | 3.001       | 9.160       |
| Equatorial radius, $R_{\text{eq}}$                                     | $R_{\odot}$        | 3.019       | 9.173       |
| Radii ratio, $R_{\text{eq}}/R_{\text{pole}}$                           | ...                | 1.006       | 1.001       |
| Mass, $M$  | $M_{\odot}$        | 2.735       | 9.683       |
| Luminosity   | $L_{\odot}$        | 68.464      | 25059.581   |
| Equatorial velocity, $V_{\text{eq}}$                                   | $\text{km s}^{-1}$ | 45.653      | 24.477      |
| Equatorial critical velocity, $V_{\text{eq-crit}}$                     | $\text{km s}^{-1}$ | 340.343     | 366.604     |
| Velocity ratio, $V_{\text{eq}} / V_{\text{eq-crit}}$                   | ...                | 0.134       | 0.067       |

Table 6. High-resolution Elodie spectra <sup>a</sup>

| Name         | HR   | HD     | [Fe/H] | ID name       | Resolution<br>( $\text{\AA}$ ) | BERV <sup>b</sup><br>( $\text{km s}^{-1}$ ) | HSRV <sup>c</sup><br>( $\text{km s}^{-1}$ ) |
|--------------|------|--------|--------|---------------|--------------------------------|---|---|
| $\alpha$ Cep | 8162 | 203280 | 0.11   | 19980702/0025 | 0.1321429                      | 10.60                                       | -15.8                                       |
| $\alpha$ Aql | 7557 | 187642 | ...    | 20031001/0016 | 0.1321429                      | -23.90                                      | -26.6                                       |
| $\beta$ Cas  | 21   | 432    | 0.07   | 20040119/0015 | 0.1321429                      | -18.91                                      | 4.3   |
| $\alpha$ Oph | 6556 | 159561 | ...    | 19990604/0027 | 0.1321429                      | 3.77  | 11.7  |
| $\alpha$ Leo | 3982 | 87901  | ...    | 19960430/0014 | 0.1321429                      | -28.00                                      | 5.9   |
| $\alpha$ Lyr | 7001 | 172167 | ...    | 19961124/0030 | 0.1321429                      | -9.77                                       | -20.6                                       |
| $\beta$ UMa  | 4295 | 95418  | ...    | 20040309/0031 | 0.1421429                      | -10.42                                      | -13.1                                       |
| $\eta$ UMa   | 5191 | 120315 | ...    | 20040428/0022 | 0.1321429                      | -11.21                                      | -13.4                                       |

<sup>a</sup>Spectra data retrieved from <http://atlas.obs-hp.fr/elodie>, see also Moutaka et al. (2004)<sup>b</sup>Barycentric Earth Radial Velocity from Elodie headers<sup>c</sup>Heliocentric Star Radial Velocity

## Appendix

```

0.0000000e+00 2.1721055e+00 0.0000000e+00 8.5880000e+03 1.0000000e+04 -1.0000000e+04 0.0000000e+00
2.5125628e-03 2.1721233e+00 1.5703696e+00 8.5879434e+03 9.9996951e+03 -9.9996738e+03 2.0664944e+01
5.0251256e-03 2.1721764e+00 3.1407182e+00 8.5877738e+03 9.9987805e+03 -9.9986951e+03 4.1325749e+01
7.5376884e-03 2.1722650e+00 4.7110248e+00 8.5874910e+03 9.9972562e+03 -9.9970641e+03 6.1978277e+01
1.0050251e-02 2.1723890e+00 6.2812684e+00 8.5870950e+03 9.9951224e+03 -9.9947809e+03 8.2618389e+01
1.2562814e-02 2.1725485e+00 7.8514280e+00 8.5865859e+03 9.9923794e+03 -9.9918460e+03 1.0324195e+02
1.5075377e-02 2.1727434e+00 9.4214825e+00 8.5859637e+03 9.9890274e+03 -9.9882596e+03 1.2384483e+02
1.7587940e-02 2.1729738e+00 1.0991411e+01 8.5852282e+03 9.9850667e+03 -9.9840222e+03 1.4442289e+02
2.0100503e-02 2.1732396e+00 1.2561192e+01 8.5843796e+03 9.9804979e+03 -9.9791344e+03 1.6497201e+02
2.2613065e-02 2.1735410e+00 1.4130805e+01 8.5834177e+03 9.9753214e+03 -9.9735967e+03 1.8548806e+02

```

**Figure 14.** The first ten rows of an Alderamin surface file (Alderamin\_Surface-omega.66.5parallax.dat). Columns: (1) co-latitude,  $\vartheta$ , in units of  $\pi$  radians; (2) radius,  $R(\vartheta)$ , in  $R_{\odot}$ ; (3) velocity,  $V(\vartheta)$ , in  $\text{km s}^{-1}$ ; (4) effective temperature,  $T_{\text{eff}}(\vartheta)$ , in K; (5) effective surface gravity,  $g(\vartheta)$ , in  $\text{cm s}^{-2}$ , with (6) the radial,  $g_r(\vartheta)$   $\text{cm s}^{-2}$  and (7) co-latitude,  $g_{\vartheta}(\vartheta)$ , in  $\text{cm s}^{-2}$ , components.

```

3.70410578e+01 -5.79645358e+01 6.87890062e+01 4.00000000e-07 -1.30899694e+00
3.92671145e+01 -5.70687933e+01 6.92730355e+01 4.00000000e-07 -1.28255256e+00
4.14657131e+01 -5.61211121e+01 6.97781096e+01 4.00000000e-07 -1.25610817e+00
4.36353162e+01 -5.51221548e+01 7.03028646e+01 4.00000000e-07 -1.22966379e+00
4.57744066e+01 -5.40726199e+01 7.08459210e+01 4.00000000e-07 -1.20321941e+00
4.78814887e+01 -5.29732414e+01 7.14058910e+01 4.00000000e-07 -1.17677503e+00
4.99550889e+01 -5.18247881e+01 7.19813834e+01 4.00000000e-07 -1.15033064e+00
5.19937572e+01 -5.06280629e+01 7.25710104e+01 4.00000000e-07 -1.12388626e+00
5.39960682e+01 -4.93839027e+01 7.31733916e+01 4.00000000e-07 -1.09744188e+00
5.59606217e+01 -4.80931776e+01 7.37871595e+01 4.00000000e-07 -1.07099750e+00

```

**Figure 15.** The first ten rows of an Alderamin uv track file (Alderamin\_Veritas\_u.v\_tracks\_400.0nm.txt). Columns: (1)  $u$ , east-west spatial frequency coordinate, in meters; (2)  $v$ , north-south spatial frequency coordinate, in meters; (3) projected baseline in meters; (4) wavelength,  $\lambda$ , in meters; (5) hour angle,  $h$ , in radians at each  $(u,v)$  point.

```

1 4.0028000000000000E+03 -2.865401418368982E-10
2 4.0029000000000000E+03 -2.864364538252529E-10
3 4.0030000000000000E+03 -2.851486789780759E-10
4 4.0031000000000000E+03 -2.838616270678155E-10
5 4.0032000000000000E+03 -2.822466978170877E-10
6 4.0033000000000000E+03 -2.806438073521793E-10
7 4.0034000000000000E+03 -2.781415322989476E-10
8 4.0035000000000000E+03 -2.756777678577966E-10
9 4.0036000000000000E+03 -2.735151507809417E-10
10 4.0037000000000000E+03 -2.709042497400885E-10

```

**Figure 16.** The first ten rows of an Alderamin spectrum file (MPL4000A\_to\_4299A\_Alderamin...h5.spec). Columns: (1) the row count; (2) wavelength,  $\lambda$ , in  $\text{\AA}$ ; (3) Flux, in,  $\text{erg cm}^{-2} \text{s}^{-1} \text{\AA}^{-1}$ .